





Article

The Effects of Electrochemical Hydrogen Charging on Charpy Impact Toughness and Dry Sliding Tribological Behavior of AISI 316H Stainless Steel

Ladislav Falat ^{*}, Lucia Čiripová , Ondrej Petruš, Viktor Puchý , Ivan Petryshynets, Karol Kovaľ and Róbert Džunda 

Institute of Materials Research, Slovak Academy of Sciences, Watsonova 47, 04001 Košice, Slovakia; lciripova@saske.sk (L.Č.); opetrus@saske.sk (O.P.); vpuchy@saske.sk (V.P.); ipetryshynets@saske.sk (I.P.); kkoval@saske.sk (K.K.); rdzunda@saske.sk (R.D.)

* Correspondence: lfalat@saske.sk; Tel.: +421-55-792-2447

Abstract: In this work, solution-annealed AISI 316H grade austenitic stainless steel was studied in terms of investigating the electrolytic hydrogen charging effects on the resulting Charpy impact toughness and dry sliding tribological behavior. Conventional Charpy impact bending tests were employed to study the mechanical response of the investigated material to dynamic loading conditions, whereas dry linear sliding tribological tests were used to study material friction and wear behavior. The obtained mechanical and tribological properties were correlated with corresponding fracture and tribological mechanisms, which were determined from morphological observations of fracture surfaces and tribological tracks. The applied testing procedures were individually carried out for the non-hydrogenated, hydrogen-charged, and dehydrogenated material conditions. The observed changes in individual properties due to applied hydrogen charging were rather small, which indicated the good resistance of solution-annealed AISI 316H steel against material degradation in currently used electrolytic hydrogenation conditions.

Keywords: austenitic steel; hydrogen charging; impact toughness; tribology



Citation: Falat, L.; Čiripová, L.; Petruš, O.; Puchý, V.; Petryshynets, I.; Kovaľ, K.; Džunda, R. The Effects of Electrochemical Hydrogen Charging on Charpy Impact Toughness and Dry Sliding Tribological Behavior of AISI 316H Stainless Steel. *Crystals* **2023**, *13*, 1249. <https://doi.org/10.3390/cryst13081249>

Academic Editors: Shenghu Chen and Qingsong Pan

Received: 21 July 2023

Revised: 7 August 2023

Accepted: 10 August 2023

Published: 12 August 2023



Copyright: © 2023 by the authors. Licensee MDPI, Basel, Switzerland. This article is an open access article distributed under the terms and conditions of the Creative Commons Attribution (CC BY) license (<https://creativecommons.org/licenses/by/4.0/>).

1. Introduction

Hydrogen is seen as a critical component of greening Europe's energy market to be the first carbon-neutral by 2050 worldwide [1,2]. In the context of building a hydrogen economy by the gradual transformation of the energy industry using ecological, so-called "green hydrogen" as an energy carrier, the challenge aimed at the safety and reliability of hydrogen production, storage, and distribution is becoming increasingly crucial [3–6]. From the viewpoint of the use of suitable metallic materials for constructing any equipment exposed to hydrogen, it is necessary to consider the eventual possibility of the occurrence of a material degradation phenomenon called hydrogen embrittlement (HE) or hydrogen-induced cracking (HIC). This type of degradation refers to the environmental embrittlement of metallic materials by the action of atomic hydrogen with the ability to diffuse into the microstructure of metals from the surrounding environment, even at room temperature [7–10]. Although intensive research on hydrogen embrittlement has been carried out for several decades, it cannot be concluded that there exists a single universal mechanism to explain the action of hydrogen in microstructures of various materials. Nevertheless, it is well-known that a key role in terms of the interaction of diffusible hydrogen with the microstructure having a decisive effect on materials' susceptibility to HE is played by so-called "hydrogen traps", which are formed by various microstructural or substructural objects capable of attracting and trapping free atomic hydrogen. These traps are various defects of the metal crystal lattice (e.g., dislocations, vacancies, substitution atoms, precipitates, inclusions, etc.) showing the existence of internal stresses in their surroundings [11–18]. Thus, there are

significant differences in the HE resistance among different classes of metallic materials taking into account not only their varying chemical compositions but also their various processing and service conditions influencing their crystallographic structures and phase composition characteristics.

In our previously published works [19–24], we investigated the effects of various conditions of heat treatment, including long-term isothermal expositions and the electrolytic hydrogen charging of welded joints of advanced creep-resistant steels on their mechanical and brittle–fracture properties. In these complex material systems, certain small improvements in HE resistance were observed after laboratory high-temperature aging experiments, which could be explained by internal stress relieving as well as by the additional precipitation of fine carbide particles leading to irreversible hydrogen trapping at carbide/matrix interfaces [19–24]. However, at the same time, the gradual development of thermal embrittlement was clearly observed due to the precipitate coarsening of several secondary phases (e.g., special alloy carbides and intermetallic phases) with the increasing duration of thermal exposure. The results of our recent study [25] about the HE behavior of plastically pre-strained and cathodically hydrogen-charged AISI 316H austenitic stainless steel have shown that this material was subjected to room-temperature static tensile testing in its solution-annealed (precipitation-free) material condition and showed rather small susceptibility to HE and its tendency for HE with increasing the plastic pre-straining was only slightly increased. It has been concluded that the observed degradation of deformation properties of plastically pre-strained and hydrogen-charged materials was predominantly caused not by HE but by gradual plasticity exhaustion due to the excessive strain-induced generation and multiplication of slip dislocations causing deformation hardening.

The present work is aimed at a continuation of our former study [25], which was focused on the characterization of HE behavior of solution-annealed and variously pre-strained AISI 316H steel in room-temperature static tensile testing conditions. The currently performed investigation concerns the effects of cathodic hydrogen charging on the mechanical response of the same AISI 316H material in dynamic loading conditions employing Charpy impact bending tests and dry linear sliding tribological tests at room temperature. The obtained results of mechanical and tribological tests are discussed in terms of their possible correlations among microstructural features, fracture surface characteristics, and acting tribological mechanisms.

2. Experimental Materials and Methods

The input experimental material was a seamless tube (38 mm outer diameter, 6 mm wall thickness) of 1050 °C solution of annealed and water-quenched AISI 316H stainless steel. With respect to its high elemental alloying (see Table 1), this material can be regarded as non-equiatomic medium–entropy alloy, as also reported in [26].

Table 1. Chemical composition in wt.% of the investigated AISI 316H stainless steel.

Material	C	Si	Mn	Cr	Mo	Ni	Fe
AISI 316H	0.05	0.51	1.77	16.76	2.05	11.13	rest

The response of the investigated material to dynamic mechanical loading in the initial non-hydrogenated state (i.e., without hydrogen charging) and then also in the hydrogenated state (i.e., after electrochemical hydrogen charging at room temperature in a solution of 1 M HCl with 0.05M N₂H₆SO₄ at a current density of 20 mA/cm² for 24 h) was evaluated from the Charpy impact bending tests and dry linear sliding tribological tests at room temperature. The used electrolytic hydrogenation procedure was selected on the basis of our former studies [23,24], which indicated an unchanging course of deformation properties of hydrogenated steel specimens after exceeding 24 h of the hydrogen charging time, giving rise to the assumption of their full hydrogen saturation. Further details concerning the selection of currently used hydrogenation conditions are given in [25]. The electrolytic

hydrogen charging of individual specimens of investigated material was performed using the potentiostat/galvanostat model 173 (Princeton Applied Research, Oak Ridge, TN, USA).

The concentration of the absorbed hydrogen within the electrochemically hydrogenated specimen was calculated on the base of the method of hydrogen electrochemical oxidation (HEO), which was principally defined and described in [27] and has been commonly used by many other authors, e.g., [28–30]. HEO was conducted out from the solution containing $1 \text{ mol}\cdot\text{dm}^{-3}$ NaOH and $8 \text{ g}\cdot\text{dm}^{-3}$ of thiourea as a hydrogen recombination poison to avoid H_2 gas evolution, using a modular potentiostat/galvanostat Autolab Vionic (Metrohm, Utrecht, Netherlands) in conventional three-electrode cells under laboratory temperature. A hydrogenated specimen with a surface area of 6.7 cm^2 was used as a working electrode, and saturated Ag/AgCl and platinum electrodes ($1 \times 1 \text{ cm}^2$) as reference and counter electrodes, respectively. The applied potential $E = -0.9 \text{ V}$ was maintained for 1000 s to ensure complete hydrogen oxidation.

The electrochemically hydrogenated specimens for mechanical and tribological tests were shortly stored in liquid nitrogen immediately after hydrogen charging. Then, one by one, the specimens were gradually warmed up on still air to room temperature and were consecutively subjected to individual testing procedures. A schematic view of the employed sub-sized Charpy V-notch (CVN) impact bending test specimen is shown in Figure 1.

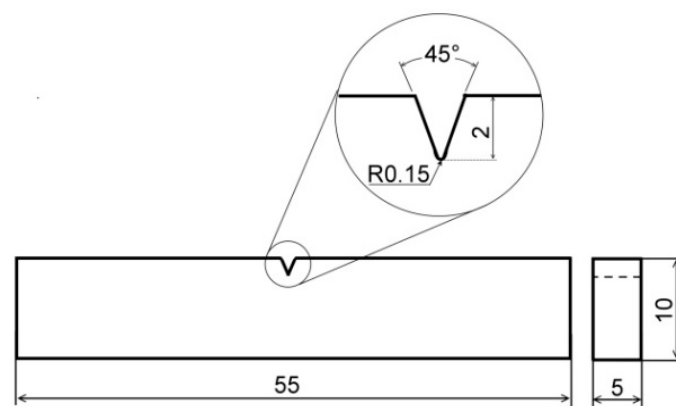


Figure 1. Schematic Charpy V-notch (CVN) impact bending test specimen. All dimensions are in mm.

A conventional Charpy pendulum impact tester PSW 30 (VEB Werkstoffprüfmaschinen Leipzig, Leipzig, Germany) with a 300 J impact energy pendulum hammer was employed to determine the CVN impact toughness in conformity with standard ISO 148-1:2016 [31]. Three individual tests were performed for each material condition. The HE resistance of the studied material was determined by the calculation of the HE index from the results of performed Charpy impact bending tests of non-hydrogenated and hydrogen-charged test specimens. The hydrogen embrittlement index (HEI) was calculated as a relative change in average CVN impact toughness values between the non-hydrogenated and hydrogen-charged test specimens according to the following formula:

$$\text{HEI}_{\text{CVN}} = \frac{\text{CVN}_0 - \text{CVN}_\text{H}}{\text{CVN}_0} \times 100\% \quad (1)$$

The subscripts “0” and “H” refer to the non-hydrogenated and hydrogen-charged material states, respectively. The dehydrogenated Charpy impact bending test specimens obtained by the long-term room-temperature holding ($25 \text{ }^\circ\text{C}/30$ days) of originally hydrogenated specimens in a dry air environment were also examined. The tribological tests were carried out on metallographically polished surfaces of the same flat prismatic samples as those used for CVN impact toughness tests. These tests were performed in the mode of dry linear sliding at room temperature using a SiC ball (5 mm diameter) counterpiece, 10 N loading force, 10 cm/s sliding speed, and 250 m sliding distance. The tribological

testing apparatus was a universal tribometer BRUKER UMT 3 (Bruker Nano GmbH, Berlin, Germany). The tribological tests were carried out in conformity with standard ASTM G133-05(2016) [32]. Vickers microhardness was measured using the microhardness tester WILSON-WOLPERT Tukon 1102 (Buehler ITW Co., Ltd., Lake Bluff, IL, USA) on a metallographically ground and polished sample surface at a 0.49 N loading force and 15 s loading time per measurement corresponding to the HV0.05 unit scale. Preliminary, microstructural observations were performed using a light optical microscope (LOM) OLYMPUS GX71 (Olympus Corporation, Tokyo, Japan). The microstructure was examined in the drawing direction of the original tube. In this direction, the samples were cut for the preparation of specimens for mechanical and tribological tests. Conventionally prepared metallographic specimens were etched in the solution of “Aqua Regia” (i.e., acidic solution of the concentrated HCl and HNO₃ acids in a molar ratio of 3:1). The grain size of studied material was determined by software ImageJ (version 1.46, National Institutes of Health, Bethesda, MD, USA). The mean grain diameter was calculated as the Feret mean diameter [33]. Detailed microstructural and fractographic analyses, including crystallographic orientation measurements and phase mapping analyses, were carried out using the scanning electron microscope (SEM) JEOL JSM-7000F (Jeol Ltd., Tokyo, Japan) linked with an electron backscatter diffraction (EBSD) detector Nordlys-I (HKL technology A/S, Hobro, Denmark). The EBSD analyses were performed on a drawing direction plane (405 µm by 315 µm in size) of prepared metallographic cross-sections, and the obtained data were processed using the software CHANNEL-5, HKL (Service pack 7). Detailed morphological observations of tribological tracks, including semi-quantitative chemical micro-analyses in selected locations, were performed using SEM TESCAN Vega-3 LMU (TESCAN Brno, s.r.o., Brno, Czech Republic) and an energy dispersive X-ray (EDX) spectrometer BRUKER XFlash Detector 410 m (Bruker Nano GmbH, Berlin, Germany). Topographical measurements of tribological profiles and specific wear rate determination were performed using a confocal microscope PLu neox 3D Optical Profiler (SENSOFAR, Barcelona, Spain) and employing a standard evaluation procedure described, for instance, in [34].

3. Results and Discussion

3.1. Microstructure of Solution-Annealed Material

A typical light-optical microstructure of solution-annealed AISI 316H steel is depicted in Figure 2, showing a polygonal grain structure with the presence of annealing twins and longitudinal inclusions in the form of dark-appearing chain-like structures. The qualitative chemical micro-analysis of these inclusions was carried out by the combination of the SEM and EDX measurement, which indicated them to be likely MnS particles (Figure 3). The more focused EDX analyses of anticipated MnS inclusions were also carried out on the fractured surfaces of broken CVN test specimens (see further in Section 3.3).

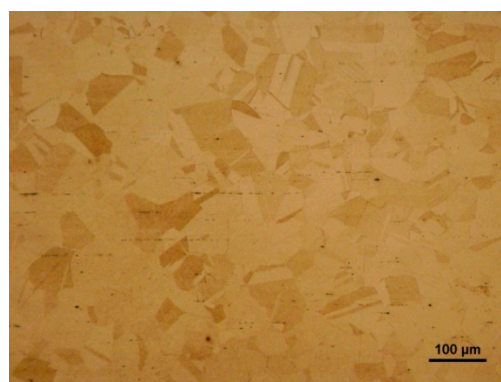


Figure 2. Light-optical micrograph of AISI 316H steel in solution-annealed material condition showing polygonal grain structure with abundant occurrence of parallel annealing twin boundaries and dark-appearing longitudinal traces of presumable MnS inclusions.

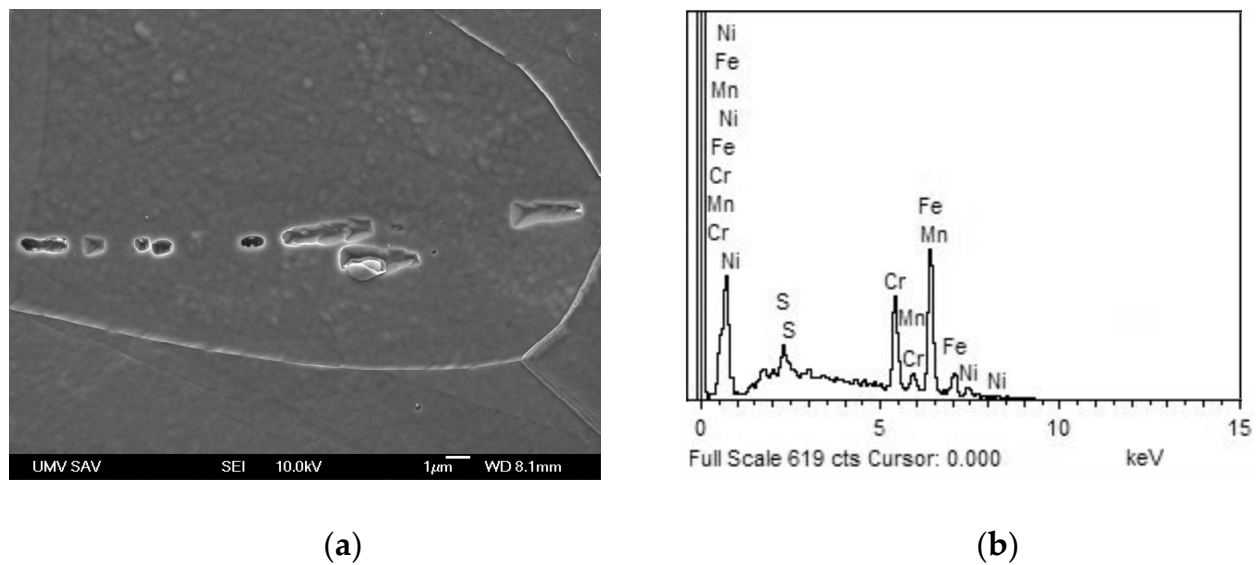


Figure 3. Higher-magnification scanning-electron micrograph of over-etched AISI 316H steel in solution-annealed material condition with typical morphology of polygonal grain boundaries and longitudinal chain-like traces of former MnS inclusions (a); typical EDX spectrum of mixed MnS trace/matrix local chemical micro-analysis (b).

The results of detailed microstructural analyses of the as-received AISI 316H material were already presented in our previous study [25]. As also shown here in Figure 2, it has been concluded that the initial material exhibited polygonal grains with the abundant occurrence of annealing twin boundaries. By means of both X-ray diffraction and EBSD phase mapping, the matrix microstructure was found to be a single-phase austenitic structure with a face-centered cubic (FCC) crystal lattice [25]. The minor occurrence of MnS inclusions was not detectable by the used techniques. The random distribution of crystallographic planes did not indicate any pronounced crystallographic texture [25].

3.2. Determination of Absorbed Hydrogen

As already stated, the concentration of the absorbed hydrogen in the CVN impact toughness test specimen was determined immediately after the process of cathodic hydrogen charging by the method of hydrogen electrochemical oxidation (HEO). The calculation of the hydrogen amount was conducted according to the formula:

$$C_H = \frac{Q_H}{zFv} \quad [\text{mol}\cdot\text{cm}^{-3}] \quad (2)$$

where Q_H is the charge value passed through the sample during anodic polarization and, in our case, at $E = -0.9$ V, z is the number of electrons in the take-in reaction, F is the Faraday constant, and v is the effective volume of the sample. In our case, we assumed that hydrogen penetrated to a depth of 1 mm, representing an effective volume of 0.67 cm^{-3} . As can be seen from Figure 4a, during the polarization of the hydrogen-charged working electrode at $E = -0.9$ V, the current drops after the first 100 s to the value closest to the zero meant that the hydrogen oxidation reaction was very fast, and after 300 s the passivation process occurred. On the other hand, the blank experiment was performed with the same sample without hydrogen charging. It is clearly visible from the red curve that in the case of the same polarization conditions, only the passivation of the sample surface occurred. Finally, the passed charge was calculated by the integration of the I-t (Figure 4b) curve in the range of 0–300 s, and the charge value was found as $Q_H = 3.63 \times 10^{-3} \text{ C}\cdot\text{cm}^{-2}$. Based on Faraday's law, it corresponds to $C_H = 3.756 \times 10^{-7} \text{ mol}\cdot\text{cm}^{-3}$. Usually, the hydrogen concentration at saturation in steel is stated in wppm. Thus, after employing corresponding

calculation procedures detailed in, e.g., [35–37], the hydrogen concentration reached a value of 0.47 wppm.

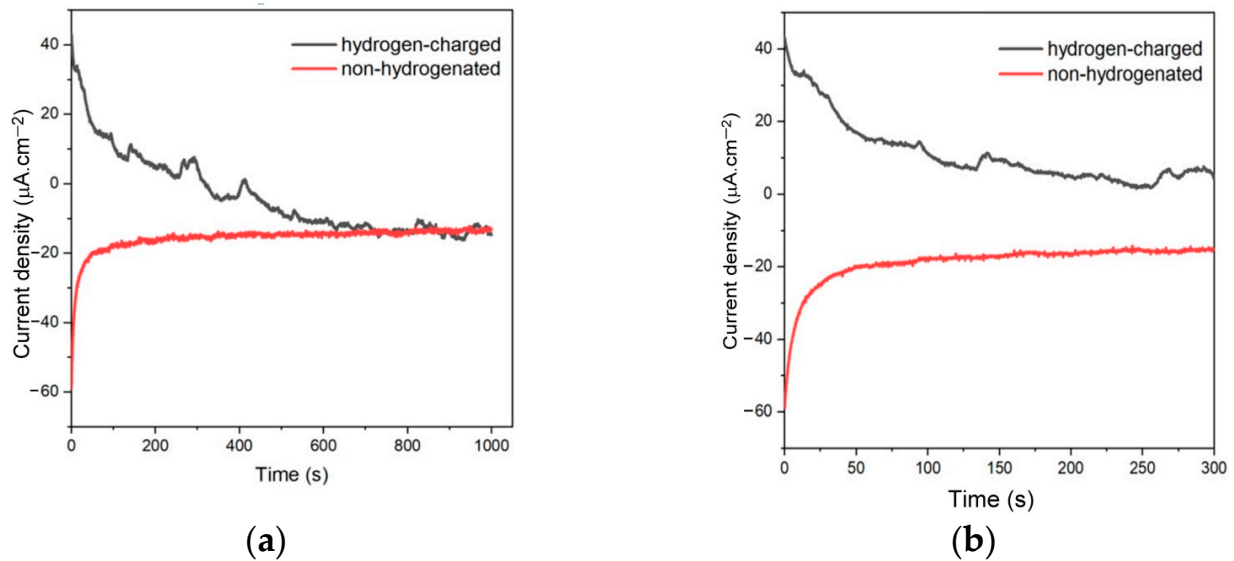


Figure 4. Potentiostatic hydrogen discharging at $E = -0.9$ V for 1000 s for the hydrogen-charged (black line) and non-hydrogenated (red line) sample (a) and zoom of the part of the I–t curve in a range of 0–300 s (b).

3.3. Effect of Hydrogen Charging on CVN Impact Toughness

Figure 5 shows the average CVN impact toughness values in non-hydrogenated, hydrogen-charged, and dehydrogenated material conditions. It can be seen that the effect of hydrogen charging on the CVN impact toughness value was rather small.

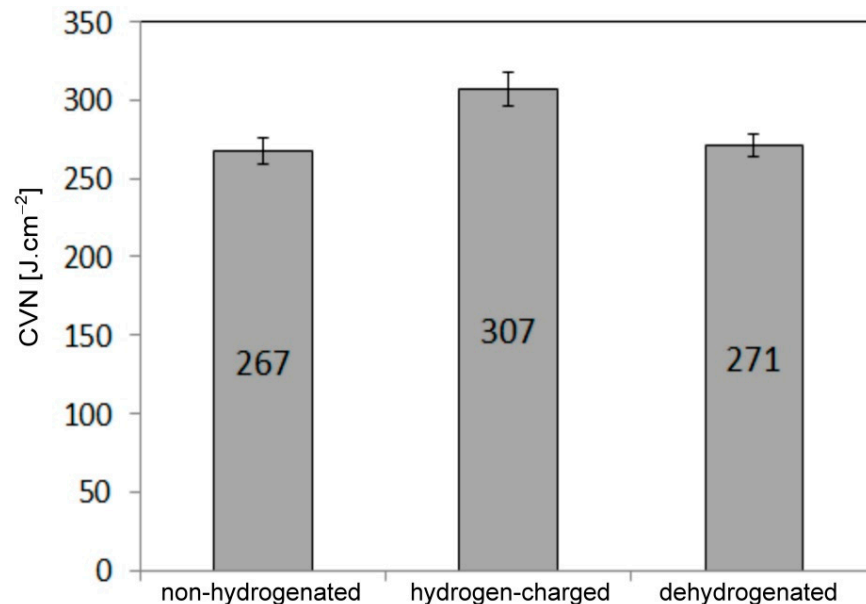


Figure 5. CVN impact toughness values of solution-annealed AISI 316H steel for individual test conditions with respect to hydrogen charging.

The comparison of individual fracture surfaces corresponding to individual material conditions did not reveal any significant differences in the fracture characteristics among individual test specimens (see Figure 6).

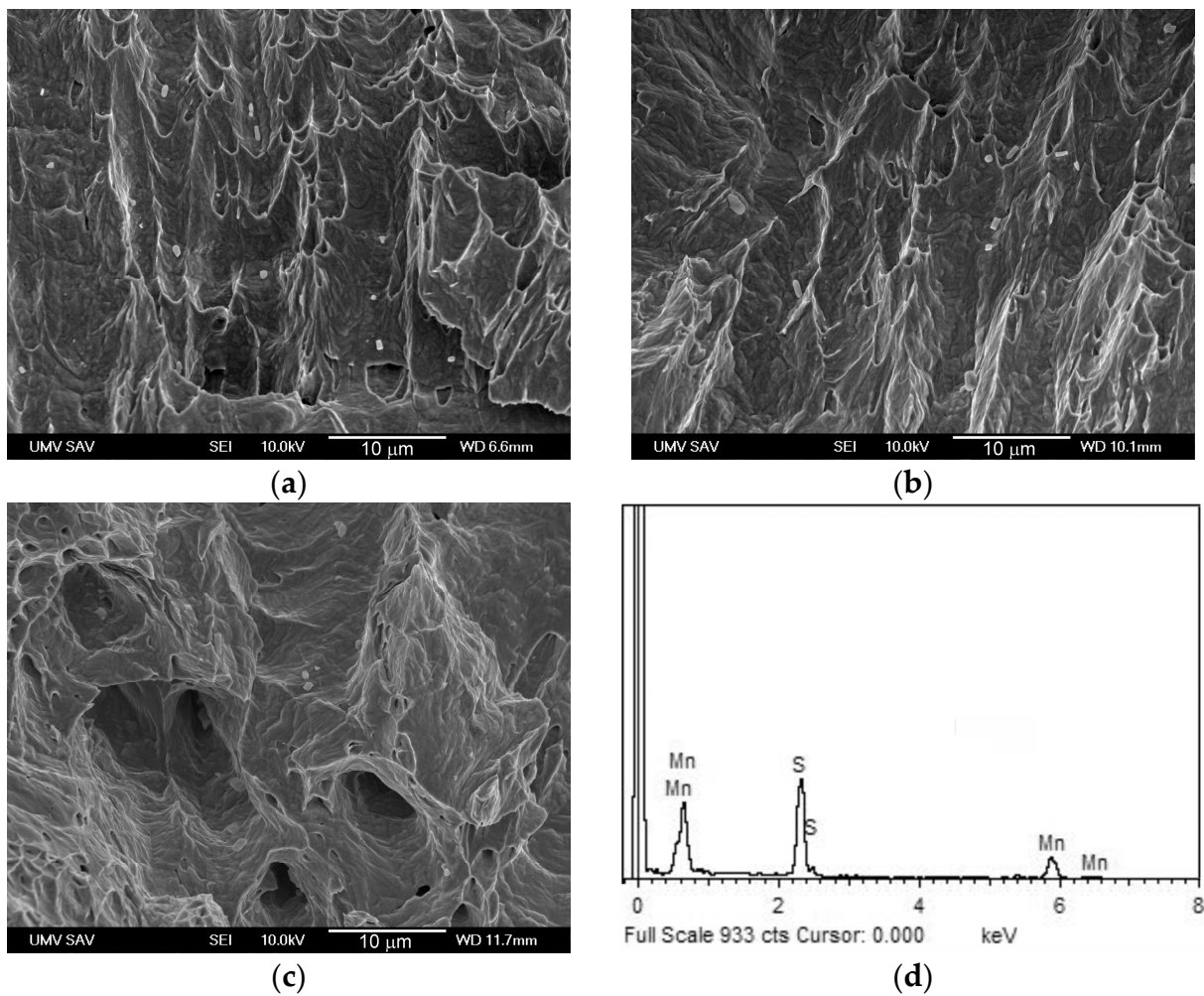


Figure 6. Scanning electron microscopic fractographs of broken CVN impact toughness test specimens of solution-annealed AISI 316H steel for individual test conditions: non-hydrogenated (a); hydrogen-charged (b); and dehydrogenated (c). Typical EDX spectrum of MnS inclusions abundantly occurring on the visualized fracture surfaces (d).

The fracture micromechanism of currently investigated material after Charpy impact bending tests was always ductile dimple tearing. The observed differences were only related to the size and morphology of individual dimples.

As already shown in Figure 5, it is interesting to note that the hydrogen-charged CVN test specimens clearly exhibited a small increase in the CVN impact toughness value compared to the non-hydrogenated test specimens. The actual occurrence of the slight toughening effect due to hydrogen charging was additionally verified by the results of the performed CVN impact toughness tests on the dehydrogenated test specimens. The obtained results clearly indicated reversibility in dynamic mechanical behavior due to the performed dehydrogenation, i.e., the possibility for the original property restoration thanks to hydrogen desorption (see Figure 5). This double-check for the results of dynamic mechanical tests of CVN test specimens without hydrogen, i.e., both the non-hydrogenated and dehydrogenated ones, strongly supports the observed findings about the occurrence of the dynamic hydrogen-toughening effect in hydrogen-charged AISI 316H material. Thus, the calculated hydrogen embrittlement index for the currently studied material resulted in a negative value, i.e., $HEI_{CVN} = -14.98\%$. The negative value of the calculated hydrogen embrittlement index might not be so surprising since, in several other studies regarding the effect of hydrogen charging on the mechanical behavior of FCC-structured alloys, similar findings have already been reported about some enhancement of deformation properties

by hydrogenation [38–47]. However, it should be noted that such behavior in relation to the enhancement of deformation properties by hydrogen charging has been typically observed in high-alloyed metallic systems, including mainly high entropy alloys with an FCC crystal structure [38–44]. From the viewpoint of the acting toughening mechanism, it has been generally accepted that the hydrogen-enhanced twinning-induced plasticity, including hydrogen-facilitated deformation nano-twinning, seemed to be the most likely mechanism of hydrogen-induced ductilization [38–47]. Murakami et al. [46] studied the fatigue behavior of 304 and 316L stainless steel and revealed their drastically improved fatigue crack growth resistance upon hydrogen charging. This behavior has been ascribed to the interplay between two competitive roles of hydrogen, namely the dislocation pinning and enhancement of dislocation mobility [46]. In the present investigation, the occurrence of deformation twinning has been clearly observed in both non-hydrogenated and hydrogen-charged test specimens after they performed CVN impact toughness bending tests (see Figure 7). Besides the clear occurrence of deformation twinning and intensive slip band formation, some random indication of sub-grains has also been observed in hydrogen-charged material (Figure 7b), which might be considered the additional toughening effect. On the contrary, no sub-grains were observed in the non-hydrogenated material (Figure 7a). The toughening effects of microstructural grain refinement are generally well-known and have been frequently reported in numerous sources in the literature, e.g., in [48–55], for various classes of structural metallic materials. However, in the case of the current investigation, it has been supposed that hydrogen charging might cause just the sub-grain visualization instead of their formation by induced hydrogen. For example, in the study [56], the origin of sub-grain formation in austenitic stainless steel was related to the specific mode of solidification. Thus, it is believed that the observed differences in the mechanical behavior of the currently studied material are mainly attributed to the higher proportion of the deformation twinning mechanism in hydrogen-charged material compared to the non-hydrogenated material (Figure 7), which also fairly agrees with the findings of [57]. The average grain sizes in terms of the Feret mean diameter for non-hydrogenated and hydrogen-charged AISI 316H material were 61 μm and 56 μm , respectively, which indicated that hydrogen-charging did not affect the material grain size significantly. Nguyen et al. [58] investigated the Charpy impact properties of hydrogen-exposed 316L stainless steel at ambient and cryogenic temperatures and found that the impact properties of their tested material had high resistance against HE. In contrast to the findings of the present investigation focused on the effects of hydrogen charging on dynamic mechanical properties of AISI 316H stainless steel, Nguyen et al. [58] observed a slight decrease in CVN impact toughness values due to hydrogen charging at all tested temperatures which were facilitated by partial phase transformation from the austenitic phase to hexagonal and cubic phases in 316L stainless steel with a modified chemical composition.

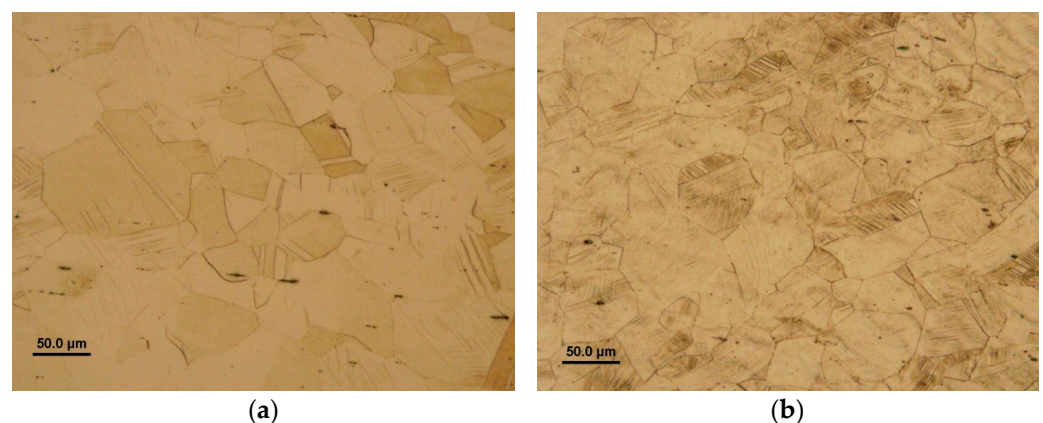


Figure 7. Light-optical micrographs of AISI 316H steel microstructure after CVN impact toughness test performed in: non-hydrogenated condition (a) and hydrogen-charged condition (b).

In Figures 8–10, the results of more focused EBSD crystallographic and phase mapping analyses from the microstructural areas just beneath the fracture locations of the specimens after CVN impact bending tests are visualized. With respect to the relatively small observed difference in measured CVN impact toughness properties between the non-hydrogenated and hydrogen-charged test specimens of the studied material, no significant microstructural differences were to be expected between the non-hydrogenated and hydrogen-charged test specimens. Figure 8 shows crystallographic microstructure visualization by inverse pole figure (IPF) imaging after a CVN impact bending test for the non-hydrogenated (Figure 8a) and hydrogen-charged (Figure 8b) CVN test specimen. Figure 8 indicates highly deformed grain microstructures with a major occurrence of near {111} crystallographic planes in addition to distinct locations exhibiting the higher occurrence of deformation twins, which are considered to enhance material toughening through the effect of twinning-induced plasticity. Due to the very high impact speed of dynamic material testing during the CVN impact bending tests of about 5.6 m/s, the considerations of the newly formed deformation twins to act like hydrogen diffusion paths could be, in this specific case, neglected.

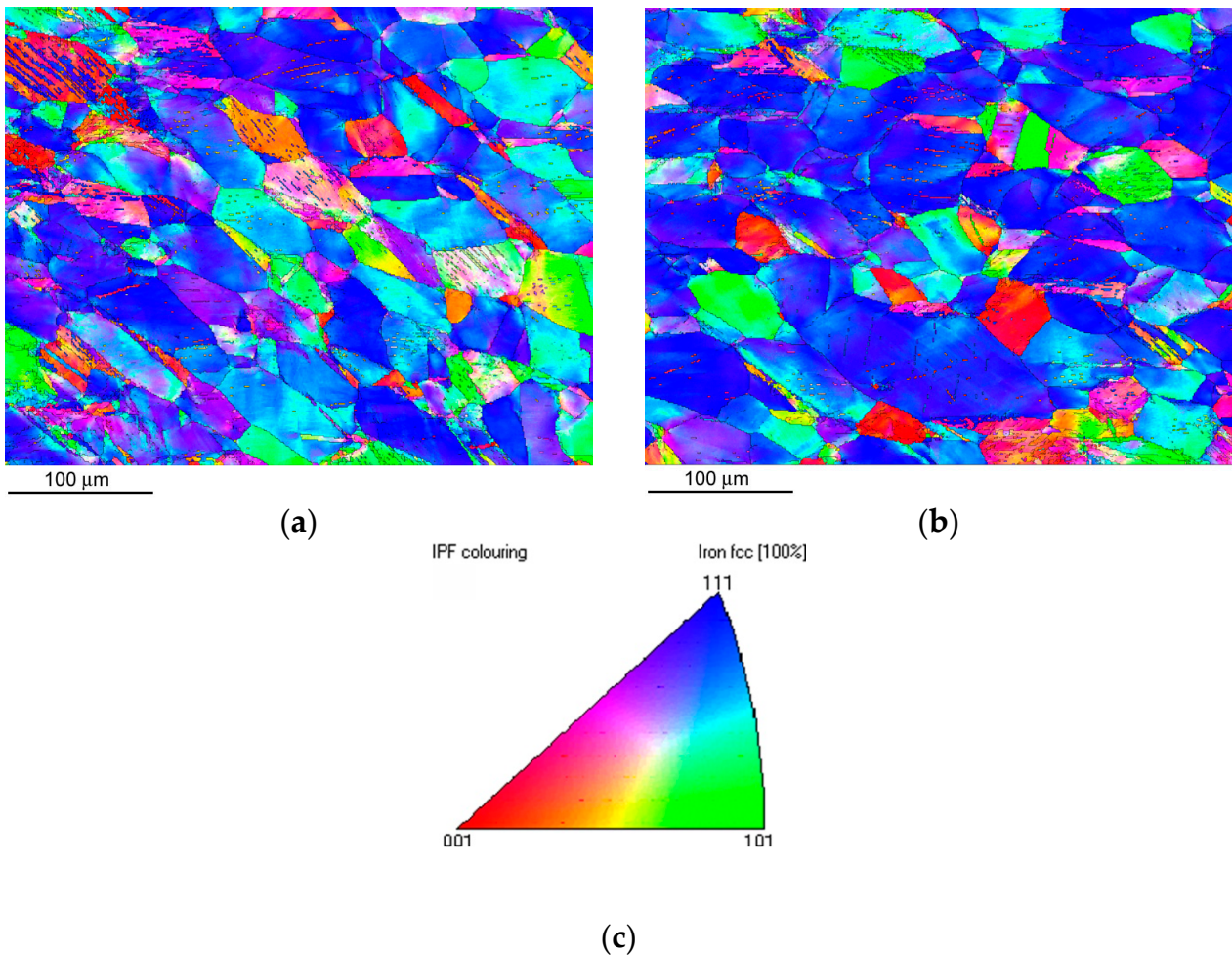


Figure 8. EBSD crystallographic microstructure visualization of AISI 316H steel by Z-direction inverse pole figure (IPF) imaging of sub-fracture surface area of a CVN impact bending test specimen in non-hydrogenated (a) and hydrogen-charged (b) material state. The legend (c) is the corresponding IPF color key.

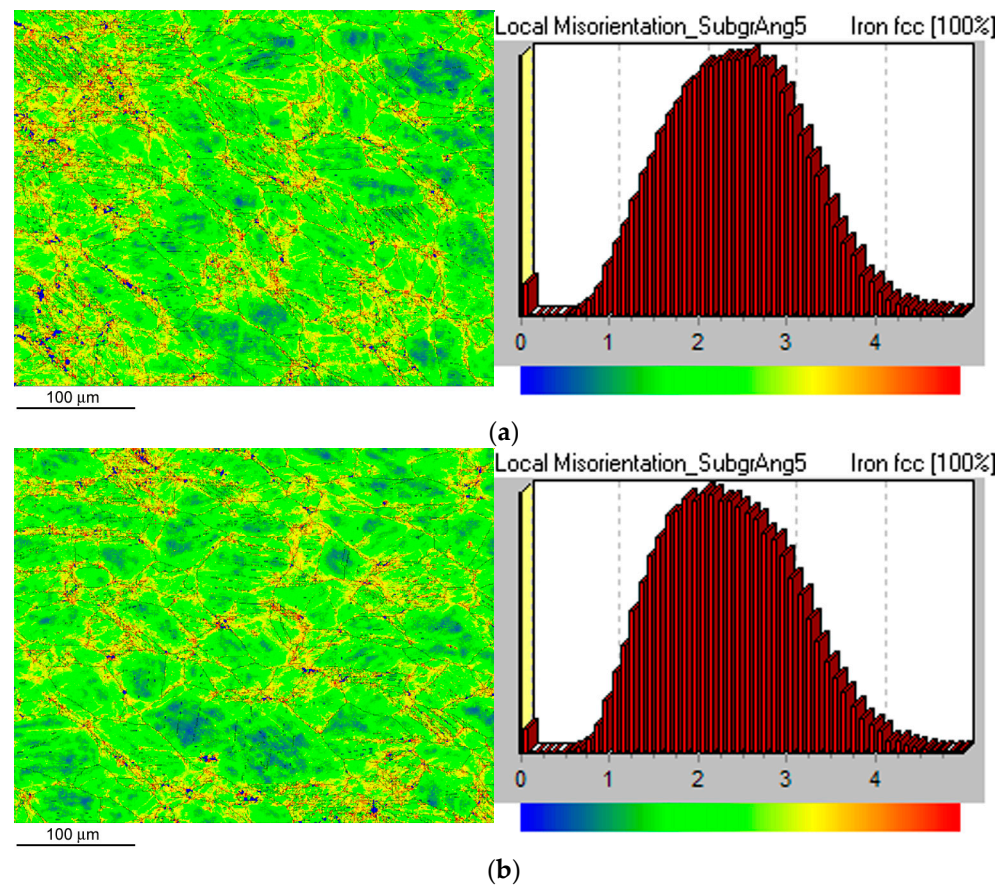


Figure 9. EBSD local misorientation mapping (LMM) microstructure visualization of AISI 316H steel in sub-fracture surface area of CVN impact bending test specimen in non-hydrogenated (a) and hydrogen-charged (b) material state. The corresponding legends (right portions) depict misorientation angle distributions.

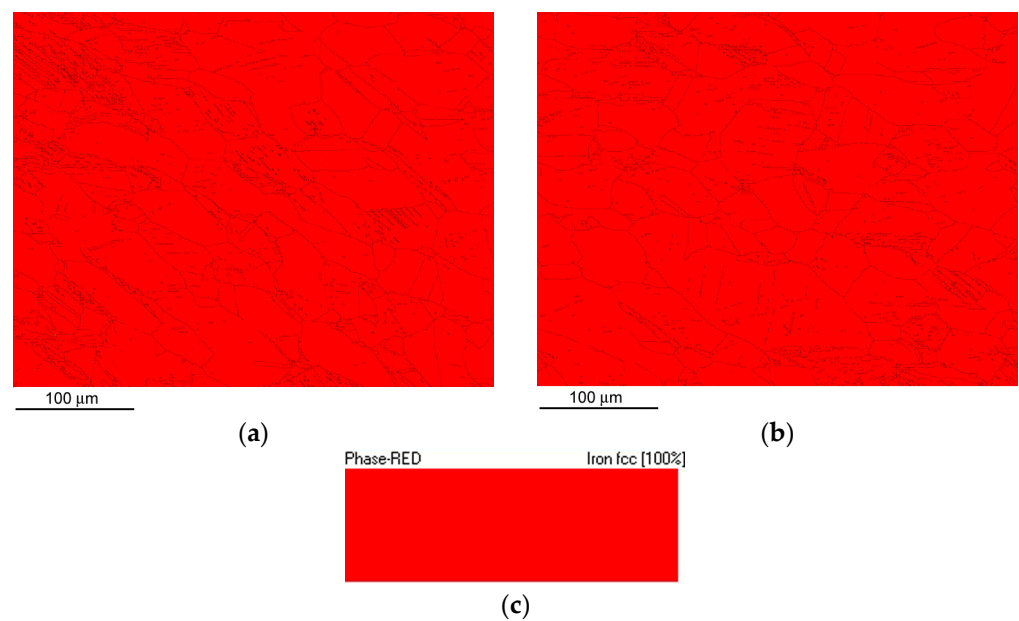


Figure 10. EBSD phase mapping microstructure visualization of AISI 316H steel in the sub-fracture surface area of the CVN impact bending test specimen in non-hydrogenated (a) and hydrogen-charged (b) material state. The legend (c) is the phase map color key.

Figure 9 shows a local misorientation map (LMM) after the CVN impact bending test for the non-hydrogenated (Figure 9a) and hydrogen-charged (Figure 9b) CVN test specimens. As expected, through the comparison of LMMs of non-hydrogenated and hydrogen-charged test specimens after the CVN impact bending tests, no significant differences in local misorientations were observed between the individual specimens (Figure 9). In other words, the areas with locally increased misorientations (yellow and red areas) indicating locally increased mechanical strains showed very similar characteristics for both material conditions, which fairly correlated with measured CVN impact toughness properties (Figure 5).

Figure 10 shows the phase mapping EBSD images for the non-hydrogenated (Figure 10a) and hydrogen-charged (Figure 10b) AISI 316H material microstructure after performing the CVN impact bending tests. The recorded phase maps (Figure 10) indicate the pure FCC austenitic crystal structure of the CVN impact on bending tested specimens in both non-hydrogenated and hydrogen-charged material conditions. This observation has shown that neither impact straining nor the electrolytic hydrogenation resulted in any phase changes in studied AISI 316H material states at room temperature.

Thus, the microstructural and supplemental EBSD analyses additionally supported conclusions regarding the observed dynamic mechanical behavior of solution-annealed AISI 316H steel, i.e., the insignificant effect of applied hydrogen charging on the resulting CVN impact toughness, which clearly indicated the very good resistance of studied material against hydrogen-related degradation in currently performed hydrogenation experiments.

3.4. Effect of Hydrogen Charging on Tribological Behavior

Figure 11 shows the average values for the coefficient of friction (COF) of studied AISI 316H material for individual material conditions with respect to the hydrogen charging application.

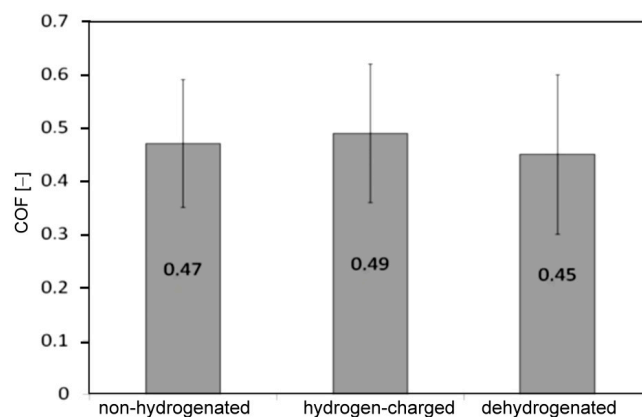


Figure 11. Average coefficients of friction of AISI 316H steel determined for its non-hydrogenated, hydrogen-charged, and dehydrogenated material states.

The results in Figure 11 indicate that the studied material in all material conditions exhibits similar average COF values. The non-hydrogenated material showed a slightly lower average COF value (0.47) than the hydrogen-charged material (0.49). The higher average COF value of hydrogen-charged AISI 316H material might be ascribed to the slight local overheating of its tribological surface due to decreased thermal conductivity by the presence of hydrogen. Indeed, it has been reported that for pure metals and alloys, thermal conductivity is reduced due to the insertion of hydrogen atoms, which hinders the thermal conduction of free electrons [59]. Such behavior was also confirmed by Luo et al. [60] in their first-principles study dealing with the effect of interstitial hydrogen on the mechanical and thermal properties of tungsten. Thus, it can be assumed that increasing COF values in currently hydrogenated AISI 316H steel is likely attributed to the fact that the hydrogen absorbed within surface layers decreases the material thermal conductivity, leading to local superheating and, consequently, the change in tribological behavior. For the sake

of completeness, the dehydrogenated material was also tribologically tested (Figure 11), and it was found that its measured average COF value decreased (0.45) compared to the COF values of the non-hydrogenated (0.47) and hydrogen-charged materials (0.49). This observed decrease in the COF value of the dehydrogenated material was likely ascribed to the mitigation of the hydrogen-related decrease in thermal conductivity in superficial layers after the dehydrogenation of studied material as well as additional surface oxidation serving as a solid lubricating agent during tribological testing [61,62].

Figure 12 displays the characteristic tribological track profiles related to individual dry linear sliding tests of studied AISI 316H steel in different material conditions. In the case of non-hydrogenated material (Figure 12a), the pure abrasive wear track can be indicated, whereas, in the other two cases (i.e., the hydrogen-charged and dehydrogenated materials) the position of the wear profile in relation to the contact area can indicate a combined abrasive–adhesive wear behavior (Figure 12b,c).

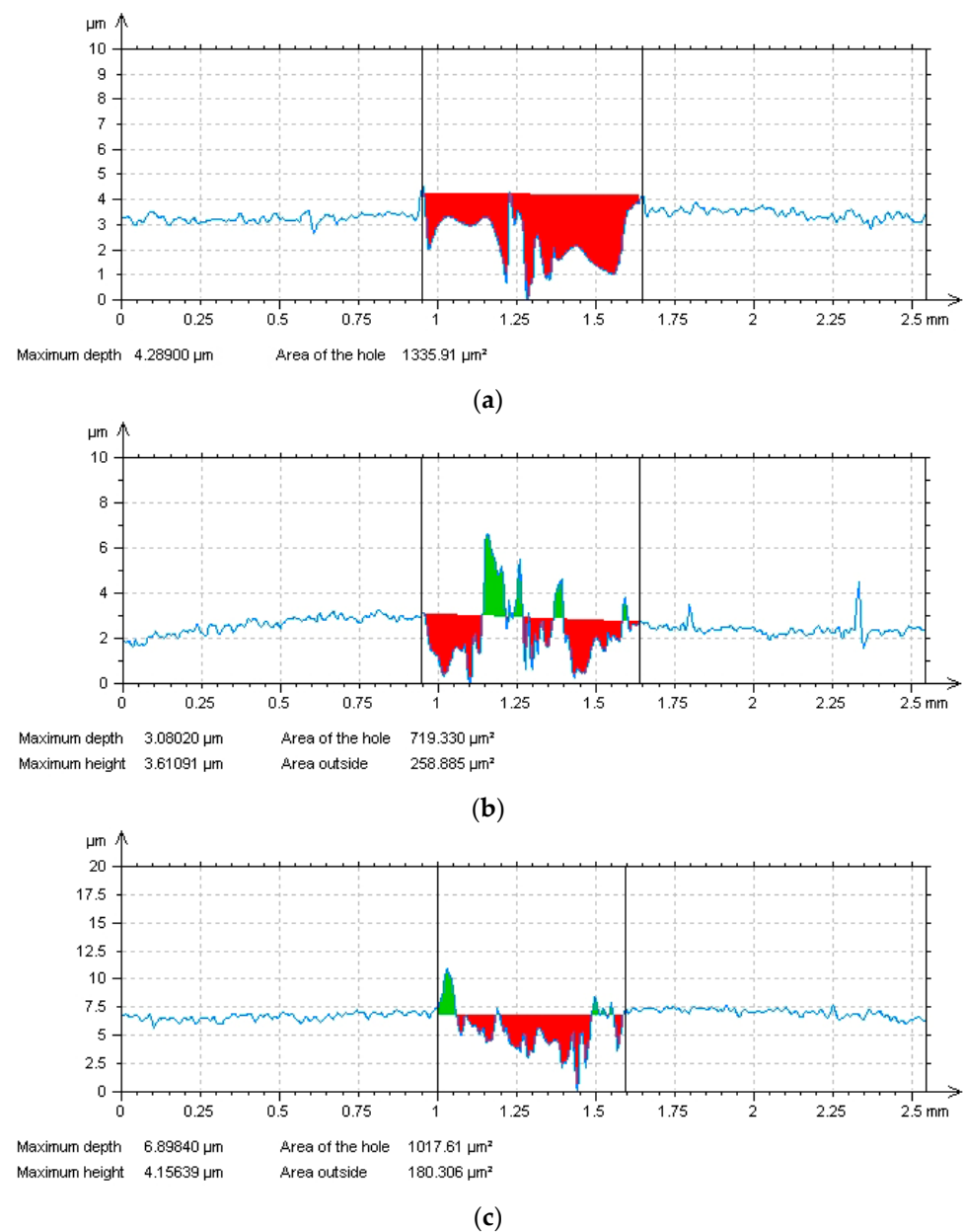


Figure 12. Characteristic tribological track profiles of studied AISI 316H material: non-hydrogenated material (a), hydrogen-charged material (b), dehydrogenated material (c).

Figure 13 shows the average values of the specific wear rates of studied AISI 316H material for individual material conditions with respect to the hydrogen charging application.

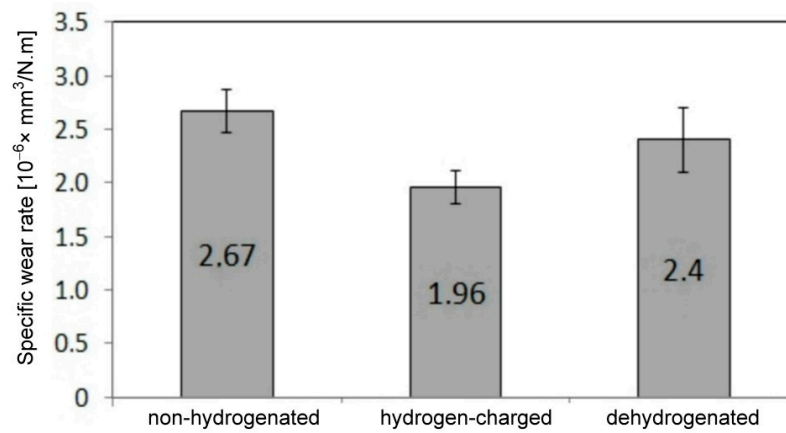


Figure 13. Average specific wear rates of studied 316H material determined for its non-hydrogenated, hydrogen-charged, and dehydrogenated material states.

The highest wear rate was shown in non-hydrogenated material (Figure 13), which exhibited a pure abrasive wear mechanism (Figure 12a). In contrast, both the hydrogen-charged and dehydrogenated materials exhibited much lower wear rates compared with the non-hydrogenated material (Figure 13), which is probably caused by their complex abrasive-adhesive wear mechanism (Figure 12b,c).

Figure 14 shows the average microhardness values of studied AISI 316H material for individual material conditions with respect to the hydrogen charging application.

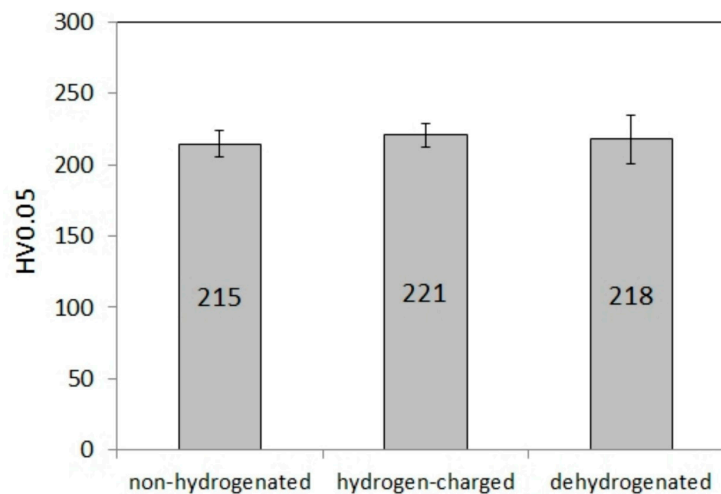


Figure 14. Average microhardness values of studied 316H material determined for its non-hydrogenated, hydrogen-charged, and dehydrogenated material states.

The lowest hardness of the non-hydrogenated material (215 HV0.05) correlated well with its highest specific wear rate ($2.67 \times 10^{-6} \text{ mm}^3/\text{N.m}$), and vice versa, i.e., the highest microhardness of the hydrogen-charged material (221 HV0.05) correlated well with its lowest specific wear rate ($1.96 \times 10^{-6} \text{ mm}^3/\text{N.m}$). Finally, the dehydrogenated material exhibited medium values of microhardness and specific wear rate (218 HV0.05 and $2.4 \times 10^{-6} \text{ mm}^3/\text{N.m}$) in comparison with non-hydrogenated and hydrogen-charged materials.

The morphological characteristics of individual tribological tracks are shown in more detail on the SEM images in Figure 15.

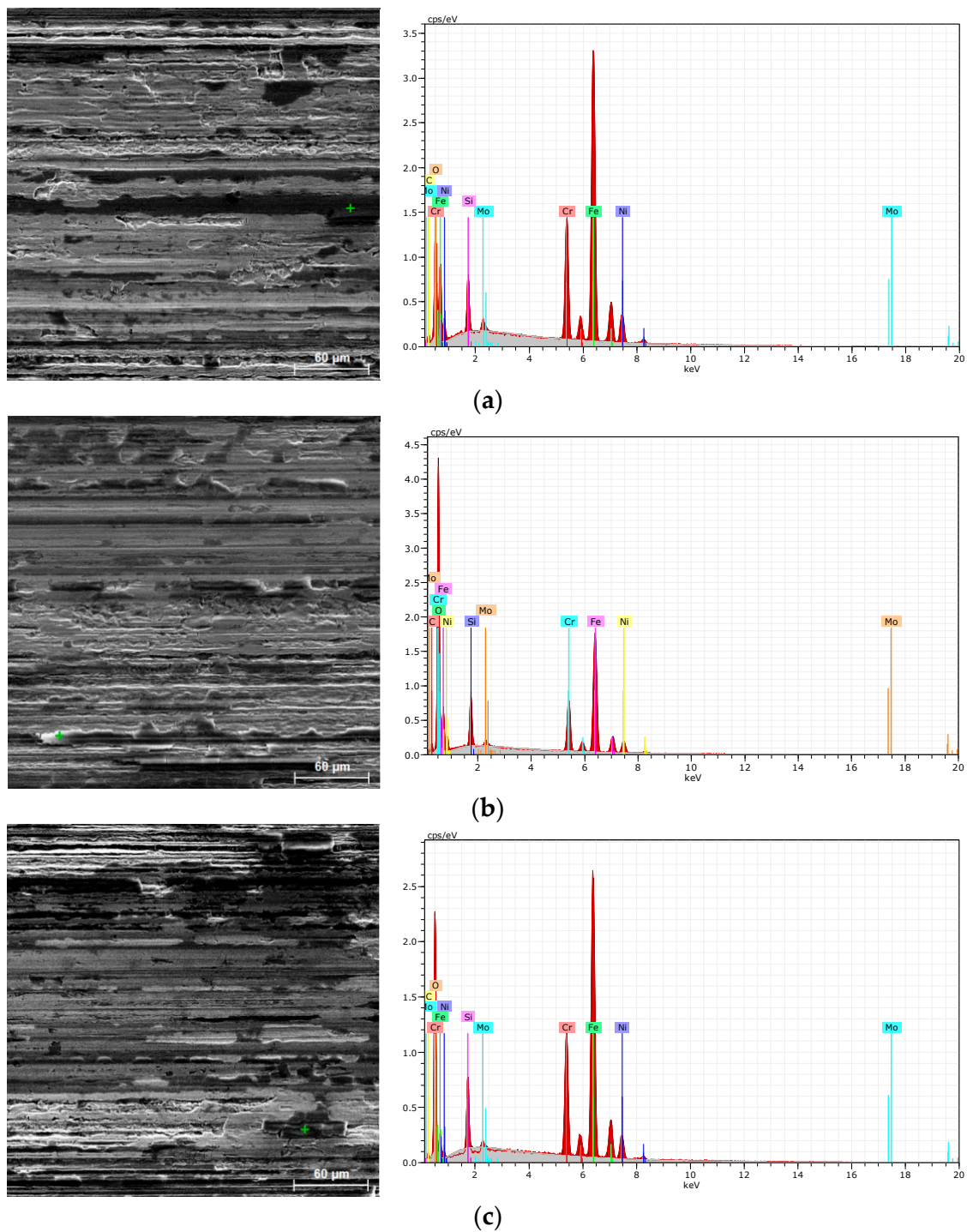


Figure 15. SEM morphological characterizations of tribological tracks including the EDX spectra of performed chemical micro-analyses of selected (marked by green cross) locations: non-hydrogenated material (a), hydrogen-charged material (b), dehydrogenated material (c).

From Figure 15, it can be concluded that all investigated material states exhibited morphologically similar tribological behavior, characterized by plastic deformation and the tribo-oxidation reaction of the steel substrate alongside the regular occurrence of SiC debris of the tribological ball counter-piece coming out of the tribological track surface, as indicated by SEM/EDX analyses. On the whole, it can be stated that the results of tribological tests supported the rest of the findings of the present investigation, pointing out that the hydrogen-charging of fully-recrystallized AISI 316H steel led to small effects on

the investigated properties studied under dynamic loading conditions, thus indicating the very good resistance of studied material against hydrogen-related degradation in currently applied electrolytic hydrogenation conditions.

4. Summary and Conclusions

Room-temperature mechanical and tribological testing procedures in correlation with microstructural analyses were employed to characterize the applied hydrogen charging effects on AISI 316H grade material. Thus, the following conclusions are summarized:

- The EBSD crystallographic phase analyses indicated that the applied electrochemical hydrogen charging and subsequent dynamic loading tests did not result in any phase transformations of the studied austenitic steel at room temperature.
- The used electrochemical hydrogen charging of investigated material resulted in a slight increase in both the CVN impact toughness and COF frictional coefficient. At the same time, the specific wear rate of electrochemically hydrogenated material exhibited a slight decrease compared to the non-hydrogenated material.
- The observed slight improvement in the CVN impact toughness of electrochemically hydrogenated AISI 316H steel is mainly related to the hydrogen-enhanced twinning-induced plasticity mechanism. However, owing to rather small changes in CVN impact toughness due to hydrogen charging, the hydrogenation effects on microstructural and fractographic characteristics were rather negligible in comparison with non-hydrogenated material.
- The COF increase in hydrogenated material could be ascribed to the local overheating of the tribological surface due to decreased thermal conductivity in the presence of hydrogen. This conclusion can be supported by the observed transition of the acting wear mechanism from pure abrasive wear for non-hydrogenated material to the more complex abrasion/adhesion wear mechanism for the hydrogen-charged material. These changes in specific wear rates for individual material states also correlate well with observed changes in acting wear mechanisms.
- Both CVN impact toughness tests and dry linear sliding tests performed on the dehydrogenated materials indicated their reversible behavior leading to the restoration of nearly original properties. On the whole, it can be concluded that the observed hydrogen-induced changes in individual properties determined under dynamic loading conditions indicated the high resistance of studied solution-annealed AISI 316H steel against material degradation in currently performed electrolytic hydrogen-charging experiments.

Author Contributions: Conceptualization, L.F.; methodology, L.Č., V.P., I.P. and O.P.; formal analysis, L.F.; investigation, L.F., L.Č., O.P., V.P., I.P., K.K. and R.D.; data curation, L.Č., O.P., V.P. and I.P.; writing—original draft preparation, L.F. and L.Č.; writing—review and editing, L.F. and L.Č.; visualization, L.Č., O.P. and I.P.; supervision, L.F.; project administration, L.F.; funding acquisition, L.F. All authors have read and agreed to the published version of the manuscript.

Funding: This work was supported by the Scientific Grant Agency of the Ministry of Education, Science, Research and Sport of the Slovak Republic and the Slovak Academy of Sciences, project VEGA 2/0072/22. The research was also supported by the Slovak Research and Development Agency under the Contract No. APVV-20-0299.

Data Availability Statement: Not applicable.

Acknowledgments: The authors cordially wish to thank M. Strečková (IMR SAS, Košice, Slovakia) for the possibility of using modular potentiostat/galvanostat Autolab Vionic and helpful discussions. The authors are also grateful to M. Džupon (IMR SAS, Košice, Slovakia) for his assistance by mechanical tests and helpful discussions.

Conflicts of Interest: The authors declare no conflict of interest. The funders had no role in the design of the study; in the collection, analyses, or interpretation of data; in the writing of the manuscript; or in the decision to publish the results.

References

1. Simon, F. EU Commission Unveils ‘European Green Deal’: The Key Points. Available online: <https://www.euractiv.com/section/energy-environment/news/eu-commission-unveils-european-green-deal-the-key-points/> (accessed on 12 June 2023).
2. Kušnířová, K.; Varcholová, D.; Molčanová, Z.; Ballóková, B.; Möllmer, J.; Jasmínská, N.; Lazár, M.; Brestovič, T.; Podobová, M.; Džunda, R.; et al. Multicomponent metal alloys tested for hydrogen storage. In Proceedings of the 31st International Conference on Metallurgy and Materials, Metal 2022, Brno, Czech Republic, 18–19 May 2022; pp. 339–344, Code 184827. [CrossRef]
3. Gérard, F.; Van Nuffel, L.; Smit, T.; Yearwood, J.; Černý, O.; Michalski, J.; Altmann, M. Opportunities for Hydrogen Energy Technologies Considering the National Energy & Climate Plans. Trinomics B.V. Final Report. FCH 2 JU. 2020. Available online: <https://trinomics.eu/wp-content/uploads/2020/09/Final-Report-Hydrogen-in-NECPs.pdf> (accessed on 12 June 2023).
4. Akhtar, M.S.; Khan, H.; Liu, J.J.; Na, J. Green hydrogen and sustainable development—A social LCA perspective highlighting social hotspots and geopolitical implications of the future hydrogen economy. *J. Clean. Prod.* **2023**, *395*, 136438. [CrossRef]
5. Tashie-Lewis, B.C.; Nnabuife, S.G. Hydrogen Production, Distribution, Storage and Power Conversion in a Hydrogen Economy—A Technology Review. *Chem. Eng. J. Adv.* **2021**, *8*, 100172. [CrossRef]
6. Dawood, F.; Anda, M.; Shafiullah, G.M. Hydrogen production for energy: An overview. *Int. J. Hydrog. Energy* **2020**, *45*, 3847–3869. [CrossRef]
7. Johnson, W.H. On some remarkable changes produced in iron and steel by the action of hydrogen and acids. *Proc. R. Soc. Lond.* **1875**, *23*, 168–179. [CrossRef]
8. Padhy, G.K.; Komizo, Y.I. Diffusible Hydrogen in Steel Weldments—A Status Review. *Trans. JWRI* **2013**, *42*, 39–62. [CrossRef]
9. Dwivedi, S.K.; Vishwakarma, M. Hydrogen embrittlement in different materials: A review. *Int. J. Hydrog. Energy* **2018**, *43*, 21603–21616. [CrossRef]
10. Depover, T.; Verbeken, K. The detrimental effect of hydrogen at dislocations on the hydrogen embrittlement susceptibility of Fe-C-X alloys: An experimental proof of the HELP mechanism. *Int. J. Hydrog. Energy* **2018**, *43*, 3050–3061. [CrossRef]
11. Liu, Q.; Venezuela, J.; Zhang, M.; Zhou, Q.; Atrens, A. Hydrogen trapping in some advanced high strength steels. *Corros. Sci.* **2016**, *111*, 770–785. [CrossRef]
12. Seo, H.J.; Kim, N.M.; Jo, J.W.; Lee, C.S. Effect of tempering duration on hydrogen embrittlement of vanadium-added tempered martensitic steel. *Int. J. Hydrog. Energy* **2021**, *46*, 19670–19681. [CrossRef]
13. Hagihara, Y.; Shobu, T.; Hisamori, N.; Suzuki, H.; Takai, K.; Hirai, K. Delayed Fracture Using CSRT and Hydrogen Trapping Characteristics of V-bearing High-strength Steel. *ISIJ Int.* **2012**, *52*, 298–306. [CrossRef]
14. Escobar, D.P.; Verbeken, K.; Duprez, L.; Verhaege, M. Evaluation of hydrogen trapping in high strength steels by thermal desorption spectroscopy. *Mater. Sci. Eng. A* **2012**, *551*, 50–58. [CrossRef]
15. Hadžipašić, A.B.; Malina, J.; Malina, M. The influence of microstructure on hydrogen diffusion and embrittlement of fine-grained high strength dual-phase steels. *Kov. Mater.* **2021**, *59*, 69–78. [CrossRef]
16. Bai, S.; Liu, L.; Liu, C.; Xie, C. Phase-Field Insights into Hydrogen Trapping by Secondary Phases in Alloys. *Materials* **2023**, *16*, 3189. [CrossRef] [PubMed]
17. Moshtaghi, M.; Safyari, M.; Mori, G. Combined thermal desorption spectroscopy, hydrogen visualization, HRTEM and EBSD investigation of a Ni-Fe-Cr alloy: The role of hydrogen trapping behavior in hydrogen-assisted fracture. *Mater. Sci. Eng. A* **2022**, *848*, 143428. [CrossRef]
18. Toribio, J.; Lorenzo, M.; Aguado, L. Innovative Design of Residual Stress and Strain Distributions for Analyzing the Hydrogen Embrittlement Phenomenon in Metallic Materials. *Materials* **2022**, *15*, 9063. [CrossRef]
19. Čiripová, L.; Falat, L.; Homolová, V.; Džupon, M.; Džunda, R.; Dlouhý, I. The Effect of Electrolytic Hydrogenation on Mechanical Properties of T92 Steel Weldments under Different PWHT Conditions. *Materials* **2020**, *13*, 3653. [CrossRef]
20. Ševc, P.; Falat, L.; Čiripová, L.; Džupon, M.; Vojtko, M. The Effects of Electrochemical Hydrogen Charging on Room-Temperature Tensile Properties of T92/TP316H Dissimilar Weldments in Quenched-and-Tempered and Thermally-Aged Conditions. *Metals* **2019**, *9*, 864. [CrossRef]
21. Falat, L.; Čiripová, L.; Homolová, V.; Kroupa, A. The influence of isothermal ageing and subsequent hydrogen charging at room temperature on local mechanical properties and fracture characteristics of martensitic-bainitic weldments for power engineering. *J. Min. Metall. Sect. B-Metall.* **2017**, *53*, 373–382. [CrossRef]
22. Falat, L.; Čiripová, L.; Homolová, V.; Futáš, P.; Ševc, P. Hydrogen pre-charging effects on the notch tensile properties and fracture behaviour of heat-affected zones of thermally aged welds between T24 and T92 creep-resistant steels. *Kov. Mater.* **2016**, *54*, 417–427. [CrossRef]
23. Blach, J.; Falat, L. The influence of thermal exposure and hydrogen charging on the notch tensile properties and fracture behaviour of dissimilar T91/TP316H weldments. *High Temp. Mater. Proc.* **2014**, *33*, 329–337. [CrossRef]
24. Blach, J.; Falat, L.; Ševc, P. The influence of hydrogen charging on the notch tensile properties and fracture behaviour of dissimilar weld joints of advanced Cr-Mo-V and Cr-Ni-Mo creep-resistant steels. *Eng. Fail. Anal.* **2011**, *18*, 485–491. [CrossRef]
25. Falat, L.; Čiripová, L.; Petryshynets, I.; Milkovič, O.; Džupon, M.; Koval, K. Hydrogen Embrittlement Behavior of Plastically Pre-Strained and Cathodically Hydrogen-Charged 316H Grade Austenitic Stainless Steel. *Crystals* **2022**, *12*, 1419. [CrossRef]
26. Zhou, Y.; Zhou, D.; Jin, X.; Zhang, L.; Du, X.; Li, B. Design of non-equiatomic medium-entropy alloys. *Sci. Rep.* **2018**, *8*, 1236. [CrossRef]
27. Yan, M.; Weng, Y. Study on hydrogen absorption of pipeline steel under cathodic charging. *Corros. Sci.* **2006**, *48*, 432. [CrossRef]

28. Ozdirik, B.; Baert, K.; Depover, T.; Vereecken, J.; Verbeken, K.; Terry, H.; De Graeve, I. Development of an Electrochemical Procedure for Monitoring Hydrogen Sorption/Desorption in Steel. *J. Electrochem. Soc.* **2017**, *164*, C747–C757. [CrossRef]
29. Capelle, J.; Gilgert, J.; Dmytrakh, I.; Pluvinage, G. Sensitivity of pipelines with steel API X52 to hydrogen embrittlement. *Int. J. Hydrog. Energy* **2008**, *33*, 7630–7641. [CrossRef]
30. Capelle, J.; Gilgert, J.; Pluvinage, G. A fatigue initiation parameter for gas pipe steel submitted to hydrogen absorption. *Int. J. Hydrog. Energy* **2010**, *35*, 833–843. [CrossRef]
31. ISO 148-1:2016; Metallic Materials—Charpy Pendulum Impact Test—Part 1: Test Method. International Organization for Standardization: London, UK, 2016. Available online: <https://www.iso.org/standard/63802.html> (accessed on 14 May 2023).
32. ASTM G133-05(2016); Standard Test Method for Linearly Reciprocating Ball-on-Flat Sliding Wear. ASTM International: West Conshohocken, PA, USA, 2016. Available online: <https://www.astm.org/g0133-05r16.html> (accessed on 14 May 2023).
33. Walton, W. Feret's Statistical Diameter as a Measure of Particle Size. *Nature* **1948**, *162*, 329–330. [CrossRef]
34. Medved', D.; Ivor, M.; Kovalčíková, A.; Múdra, E.; Csanádi, T.; Sedlák, R.; Ünsal, H.; Tatarko, P.; Tatarková, M.; Šajgalík, P.; et al. Wear behavior of (Mo–Nb–Ta–V–W)C high-entropy carbide. *Int. J. Appl. Ceram. Technol.* **2023**, *20*, 224–235. [CrossRef]
35. Pearson, T. Calculation of the Amount of Hydrogen Absorbed by Steel During the Mechanical Plating Operation. MacDermid Industrial Solutions 4/2/2015. Available online: <https://anochrome.com/wp-content/uploads/Embrittlement-in-Mech.pdf> (accessed on 9 July 2023).
36. Lovicu, G.; Bottazzi, M.; D'aiuto, F.; De Sanctis, M.; Dimatteo, A.; Santus, C.; Valentini, R. Hydrogen embrittlement of automotive advanced high-strength steels. *Metall. Mater. Trans. A* **2012**, *43*, 4075–4087. [CrossRef]
37. Cho, S.; Kim, G.-I.; Ko, S.-J.; Yoo, J.-S.; Jung, Y.-S.; Yoo, Y.-H.; Kim, J.-G. Comparison of Hydrogen Embrittlement Susceptibility of Different Types of Advanced High-Strength Steels. *Materials* **2022**, *15*, 3406. [CrossRef]
38. Luo, H.; Li, Z.; Raabe, D. Hydrogen enhances strength and ductility of an equiatomic high-entropy alloy. *Sci. Rep.* **2017**, *7*, 9892. [CrossRef]
39. Feng, Z.; Li, X.; Song, X.; Gu, T.; Zhang, Y. Hydrogen Embrittlement of CoCrFeMnNi High-Entropy Alloy Compared with 304 and IN718 Alloys. *Metals* **2022**, *12*, 998. [CrossRef]
40. Zhang, S.; Liu, M.; Luo, Y.; Wang, L.; Wang, Z.; Wang, Z.; Li, F.; Wang, X. Immunity of Al0.25CoCrFeNi high-entropy alloy to hydrogen embrittlement. *Mater. Sci. Eng. A* **2021**, *821*, 141590. [CrossRef]
41. Mohammadi, A.; Novelli, M.; Arita, M.; Bae, J.W.; Kim, H.S.; Grosdidier, T.; Edalati, K. Gradient-structured high-entropy alloy with improved combination of strength and hydrogen embrittlement resistance. *Corros. Sci.* **2022**, *200*, 110253. [CrossRef]
42. Pu, Z.; Chen, Y.; Dai, L.H. Strong resistance to hydrogen embrittlement of high-entropy alloy. *Mater. Sci. Eng. A* **2018**, *736*, 156–166. [CrossRef]
43. Kwon, Y.J.; Won, J.W.; Park, S.-H.; Lee, J.H.; Lim, K.R.; Na, Y.S.; Lee, C.S. Ultrahigh-strength CoCrFeMnNi high-entropy alloy wire rod with excellent resistance to hydrogen embrittlement. *Mater. Sci. Eng. A* **2018**, *732*, 105–111. [CrossRef]
44. Zhao, Y.; Lee, D.H.; Kim, W.J.; Seok, M.Y.; Kim, J.Y.; Han, H.N.; Suh, J.Y.; Ramamurty, U.; Jang, J.I. Influence of pre-strain on the gaseous hydrogen embrittlement resistance of a high-entropy alloy. *Mater. Sci. Eng. A* **2018**, *718*, 43–47. [CrossRef]
45. Lai, Z.H.; Lin, Y.T.; Sun, Y.H.; Tu, J.F.; Yen, H.W. Hydrogen-induced ductilization in a novel austenitic lightweight TWIP steel. *Scr. Mater.* **2022**, *213*, 114629. [CrossRef]
46. Murakami, Y.; Kanazaki, T.; Mine, Y. Hydrogen Effect against Hydrogen Embrittlement. *Metall. Mater. Trans. A* **2010**, *41*, 2548–2562. [CrossRef]
47. Ueki, S.; Oura, R.; Mine, Y.; Takashima, K. Micro-mechanical characterisation of hydrogen embrittlement in nano-twinned metastable austenitic stainless steel. *Int. J. Hydrog. Energy* **2020**, *45*, 27950–27957. [CrossRef]
48. Li, X.; Lu, G.; Wang, Q.; Zhao, J.; Xie, Z.; Misra, R.D.K.; Shang, C. The Effects of Prior Austenite Grain Refinement on Strength and Toughness of High-Strength Low-Alloy Steel. *Metals* **2022**, *12*, 28. [CrossRef]
49. Li, X.; Zhao, J.; Dong, L.; Misra, R.D.K.; Wang, X.; Wang, X.; Shang, C. The Significance of Coherent Transformation on Grain Refinement and Consequent Enhancement in Toughness. *Materials* **2020**, *13*, 5095. [CrossRef]
50. Park, M.; Kang, M.S.; Park, G.-W.; Choi, E.Y.; Kim, H.-C.; Moon, H.-S.; Jeon, J.B.; Kim, H.; Kwon, S.-H.; Kim, B.J. The Effects of Recrystallization on Strength and Impact Toughness of Cold-Worked High-Mn Austenitic Steels. *Metals* **2019**, *9*, 948. [CrossRef]
51. Liao, J.; Hotta, M.; Kaneko, K.; Kondoh, K. Enhanced impact toughness of magnesium alloy by grain refinement. *Scr. Mater.* **2009**, *61*, 208–211. [CrossRef]
52. Karthikeyan, T.; Thomas Paul, V.; Saroja, S.; Moitra, A.; Sasikala, G.; Vijayalakshmi, M. Grain refinement to improve impact toughness in 9Cr–1Mo steel through a double austenitization treatment. *J. Nucl. Mater.* **2011**, *419*, 256–262. [CrossRef]
53. Zhang, W.; Dong, Z.H.; Shang, X.; Chen, S.G.; Zhang, L.J.; Peng, X. Enhancement of the strength-toughness balance in a quenched laser-additively-manufactured low alloy mild steel: Effect of grain refinement and nanotwin bundle formation. *Mater. Sci. Eng. A* **2023**, *862*, 144488. [CrossRef]
54. Zhang, S.; Yang, M.; Wu, X.; Yuan, F. Superior fracture toughness with high yield strength in a high-Mn steel induced by heterogeneous grain structure. *Mater. Des.* **2023**, *225*, 111473. [CrossRef]
55. Stavrovskaia, V.E.; Efremenko, V.G.; Zurnadzhly, V.I.; Zotov, D.S.; Sagirov, R.I.; Chabak Yu, G.; Brykov, M.N.; Efremenko, B.V. Effect of Chemical Composition and Normalization Parameters on Microstructure and Mechanical Properties of Microalloyed Sheet Steel for Structural Purposes. In *Advances in Materials Science Research*; Wythers, M.C., Ed.; Nova Science Publishers, Inc.: New York, NY, USA, 2022; Volume 55, ISBN 979-8-88697-213-9.

56. Rahimi, R.; Biermann, H.; Volkova, O.; Mola, J. On the origin of subgrain boundaries during conventional solidification of austenitic stainless steels. *IOP Conf. Ser. Mater. Sci. Eng.* **2018**, *373*, 012005. [[CrossRef](#)]
57. Ogawa, Y.; Nishida, H.; Takakuwa, O.; Tsuzaki, K. Hydrogen-enhanced deformation twinning in Fe-Cr-Ni-based austenitic steel characterized by in-situ EBSD observation. *Mater. Today Commun.* **2023**, *34*, 105433. [[CrossRef](#)]
58. Nguyen, L.T.H.; Hwang, J.S.; Kim, M.S.; Kim, J.H.; Kim, S.K.; Lee, J.M. Charpy Impact Properties of Hydrogen-Exposed 316L Stainless Steel at Ambient and Cryogenic Temperatures. *Metals* **2019**, *9*, 625. [[CrossRef](#)]
59. Ye, J.; Li, Z.; Zhang, L.; Wang, S.; Jiang, L. Measurement and the improvement of effective thermal conductivity for a metal hydride bed—A review. *RSC Adv.* **2022**, *12*, 25722. [[CrossRef](#)] [[PubMed](#)]
60. Luo, M.; Jiang, D.; Liu, S.; Ouyang, C. Effect of Interstitial Hydrogen on the Mechanical and Thermal Properties of Tungsten: A First-Principles Study. *J. Phys. Chem. C* **2019**, *123*, 1913–1921. [[CrossRef](#)]
61. Mittal, D.; Singh, D.; Kumar Sharma, S. Thermal Characteristics and Tribological Performances of Solid Lubricants: A Mini Review. In *Advances in Rheology of Materials*; Dutta, A., Ali, H.M., Eds.; IntechOpen: London, UK, 2023; Available online: <https://www.intechopen.com/chapters/86047> (accessed on 19 July 2023).
62. Roy, A.; Patel, P.; Sharifi, N.; Chromik, R.R.; Stoyanov, P.; Moreau, C. Binary and ternary lubricious oxides for high temperature tribological applications: A review. *Results Surf. Interfaces* **2023**, *11*, 100117. [[CrossRef](#)]

Disclaimer/Publisher’s Note: The statements, opinions and data contained in all publications are solely those of the individual author(s) and contributor(s) and not of MDPI and/or the editor(s). MDPI and/or the editor(s) disclaim responsibility for any injury to people or property resulting from any ideas, methods, instructions or products referred to in the content.